

SCIENTIFIC REPORTS



OPEN

Direct-written polymer field-effect transistors operating at 20 MHz

Andrea Perinot^{1,2}, Prakash Kshirsagar³, Maria Ada Malvindi³, Pier Paolo Pompa^{3,4}, Roberto Fiammengo³ & Mario Caironi¹

Received: 05 May 2016

Accepted: 16 November 2016

Published: 12 December 2016

Printed polymer electronics has held for long the promise of revolutionizing technology by delivering distributed, flexible, lightweight and cost-effective applications for wearables, healthcare, diagnostic, automation and portable devices. While impressive progresses have been registered in terms of organic semiconductors mobility, field-effect transistors (FETs), the basic building block of any circuit, are still showing limited speed of operation, thus limiting their real applicability. So far, attempts with organic FETs to achieve the tens of MHz regime, a threshold for many applications comprising the driving of high resolution displays, have relied on the adoption of sophisticated lithographic techniques and/or complex architectures, undermining the whole concept. In this work we demonstrate polymer FETs which can operate up to 20 MHz and are fabricated by means only of scalable printing techniques and direct-writing methods with a completely mask-less procedure. This is achieved by combining a fs-laser process for the sintering of high resolution metal electrodes, thus easily achieving micron-scale channels with reduced parasitism down to 0.19 pF mm^{-1} , and a large area coating technique of a high mobility polymer semiconductor, according to a simple and scalable process flow.

Printed organic electronics has become a widespread research field in the recent years, thanks to the increased compatibility of the fabrication techniques with flexible, low-cost substrate materials, which results in the tangible prospect of economically convenient mass production of distributed electronics^{1–4}. Notable demonstrations have been proposed for light detectors^{5,6}, sensors^{7,8}, transistors⁹, and on their integration into truly fully-printed opto-electronic circuits^{10–14}, setting a step forward in the adoption of this technology into real life. On the other hand, the enhancement of some desirable figures of merit still has to be appropriately approached to enable the implementation of a wide range of real applications. To this goal, it is of key importance to enhance the performance of the single organic transistors constituting the basic building block of almost any electronic circuitry.

Primarily, a transistor operation frequency suitable for more demanding applications must be guaranteed, e.g. several MHz at least in the case of addressing electronics for high-resolution flexible displays¹⁵, wireless communication devices^{16–18}, and RFID-based item-tracking systems^{19,20}. Yet, in the majority of works, AC operation is either not assessed or considered a secondary goal compared to DC performance, and it is only marginally developed and analyzed.

It is well established that in typical organic field-effect architectures the optimization of high-frequency operation, besides requiring the adoption of semiconducting materials guaranteeing high effective mobility^{21,22} and of dielectric layers with high relaxation frequency and yielding interfacial properties promoting efficient charge transport^{23,24}, is largely determined by the reduction of the device channel length and of gate parasitic capacitance²⁵. Nonetheless, this operation increases the influence of the charge injection limitations on the overall behavior of the device^{26–28}. Fulfilling such requirements with a mask-less and fully solution-based process flow, albeit challenging, is highly desirable for the development of cost-effective technologies for wearable, portable and distributed applications.

However, while promising results in AC operation of organic FETs have been reported, with a maximum operating frequency as high as 27.7 MHz²⁹, record values have been so far mainly achieved by adopting photolithographic steps^{30–33} and/or single crystal semiconductors³⁴. To date, one order-of-magnitude lower operating frequencies have been demonstrated when mask-less, scalable techniques were used, with a maximum of 3.3 MHz^{25,35–37}.

¹Center for Nano Science and Technology@PoliMi, Istituto Italiano di Tecnologia, via Giovanni Pascoli 70/3, Milano, Italy. ²Dipartimento di Fisica, Politecnico di Milano, Piazza Leonardo da Vinci 32, Milano, Italy. ³Center for Biomolecular Nanotechnologies@UniLe, Istituto Italiano di Tecnologia, Via Barsanti, 73010 Arnesano, Lecce, Italy. ⁴Istituto Italiano di Tecnologia, Via Morego 30, 16163 Genova, Italy. Correspondence and requests for materials should be addressed to R.F. (email: roberto.fiammengo@iit.it) or M.C. (email: mario.caironi@iit.it)

In this work, we used a complete mask-less approach for the development of fully solution-processed polymer FETs capable of operating at frequencies as high as 20 MHz. In particular, we demonstrated the successful combination of printing techniques, such as large-area bar-coating³⁸, and digital fs-laser sintering^{39–41}. The latter is a direct writing technique for the fine patterning of a specifically formulated silver nanoparticle (Ag-NP) ink that allowed the fabrication of high-resolution conductive features down to a minimum lateral size of $\sim 1.3\ \mu\text{m}$, to be used as electrodes for high performance polymer FETs.

Results

Ag-NP ink preparation. We have specifically developed a silver ink for the fs-laser sintering process, starting from the synthesis of AgNPs with narrow size distribution, using a mixture of sodium citrate and tannic acid as reducing and stabilizing agents in aqueous conditions⁴². Other synthesis protocols have been recently proposed using tannic acid for controlling nanoparticle size either in combination with sodium citrate⁴³ or by careful control of the reaction mixture pH⁴⁴. However, the reported conditions appear to be unsuitable for the preparation of AgNPs in such large amounts as required for conductive ink applications. We have, therefore, conducted an optimization of the reaction conditions and in particular temperature, reagents ratio and order of addition of the reagents, to allow the preparation of $23.8 \pm 4.0\ \text{nm}$ AgNPs (Fig. 1a and b) with a production scale-up factor between 150 and 300 times and yet of comparably narrow size distribution as those previously reported in the literature^{42–44}. In a typical synthesis, our method yields 20 times more AgNPs also with respect to the approach recently reported by Zhang and coworkers⁴⁵. After synthesis, the AgNPs were concentrated by centrifugation and coated by polyvinylpyrrolidone (PVP) of relatively low molecular weight (10 kDa). The choice of this polymer allowed us to increase the stability and processability of the AgNPs colloidal solution, while keeping thin the organic layer on the nanoparticle surface, a desirable property when aiming at conductive inks. The final AgNPs-based conductive inks have silver content of approx. 7% in water as the dispersion medium.

Fs-laser sintering process. The AgNP ink was exploited to fabricate the device electrodes, following the process flow schematically illustrated in Fig. 1c. First, a uniform film of the conductive ink is deposited onto a substrate by spin-coating. Then, a femtosecond pulsed laser beam ($\lambda = 1030\ \text{nm}$, 67 MHz repetition rate) locally heats the nanoparticle film and patterns the desired geometry of conductive features which are $\sim 70\ \text{nm}$ thick. As a final step, the unprocessed areas of the film are washed away using water, and only the conductive high-resolution patterns are left on the substrate. Differently from what previously reported in literature⁴¹, our fs-sintering process does not require any ink encapsulation prior to laser processing, thus largely simplifying the process and making it potentially scalable.

To properly control the metallic electrodes fabrication process and to determine the optimal conditions for their integration into FETs, we performed a thorough study and related the fabrication parameters, such as power (in the range 5–30 mW, corresponding to the range $0.8\text{--}4.9\ \text{mW}/\mu\text{m}^2$), scanning speed (in the range $0.05\text{--}1\ \text{mm s}^{-1}$) and magnification power of the optics (20X, 50X or 100X), to the dimensions and conductivity of the sintered patterns. We fabricated $190\ \mu\text{m}$ -long single lines varying said process parameters and measured their lateral width and electrical resistance. In Fig. 1e we relate the obtained line width with the beam power for different scanning speeds: an approximately linear dependence can be identified in the range from 5 to 30 mW, yielding linewidths from a minimum of 1.3 to $5.3\ \mu\text{m}$. A similar trend is highlighted also when testing the line width versus beam power varying the optics ($0.1\ \text{mm/s}$, Fig. 1d).

The conductivity of the laser-sintered lines was compared to the bulk-Ag conductivity for different beam power and scanning speed (Fig. 1f). A general increase of the conductivity is observed when increasing the beam power or slowing down the scanning speed, and its value ranges between 4.5 and 21 kS/cm, which corresponds to a range from 0.7 to 3.3% of bulk silver conductivity. This range is in line with the typical conductivities obtained with more established direct-writing techniques, such as inkjet printing⁴⁶. This validates the suitability of this process and ink for the fabrication of high-resolution conductive patterns for organic electronics applications.

We then employed fs-laser sintering for the fabrication of the source and drain bottom contacts of polymer FETs, in order to benefit both from the reduction of the channel length and of the width of the contacts. Previous examples where fs-laser sintered contacts were used for organic FETs are reported in refs 41,47. Such examples either did not integrate high-resolution, reduced parasitic capacitance electrodes⁴¹, or adopted more expensive Au inks⁴⁷. Both reported only bottom-gate, bottom-contacts architectures, which, while more easily accessible, are not as performing as staggered, top-gate devices for injection in downscaled channels. Indeed, very limited performance in terms of mobility were achieved (μ lower than $10^{-2}\ \text{cm}^2/\text{Vs}$ for channel lengths longer than $5\ \mu\text{m}$). Therefore, previous reports do not answer the question whether fs-laser sintering is a candidate for the fabrication of high-frequency, direct-written polymer transistors, which is the main goal of the present work.

Polymer FETs fabrication and DC characterization. We fabricated high-resolution short- and long-channel *n*-type polymer FETs in a staggered, top-gate configuration (Fig. 2d), which is known to yield better charge injection properties from the contacts²⁶. The fabrication process flow is illustrated in Fig. 2a. For the contacts, following the optimization process described above, the chosen laser processing parameters were set to 12 mW beam power ($1.9\ \text{mW}/\mu\text{m}^2$), 50X optics, $0.5\ \text{mm/s}$ scanning speed. A typical AFM image of a fabricated contact is shown in Fig. 1g. We adopted the semiconducting co-polymer poly[N,N'-bis(2-octyldecyl)-naphthalene-1,4,5,8-bis(dicarboximide)-2,6-diyl]-alt-5,5'-(2,2'-bithiophene), P(NDI2OD-T2) (Fig. 2c), which was deposited through bar-coating, a scalable large-area printing technique^{2,38}. A 500 nm-thick PMMA layer was deposited through spin-coating, and finally we selectively inkjet-printed PEDOT:PSS over the channel and contact area to create the top gate contact. We fabricated devices with different channel lengths L of 1.75, 5.1 and $21.6\ \mu\text{m}$. The contact width L_{ov} was $3.0 \pm 0.5\ \mu\text{m}$ and the channel width W was $800\ \mu\text{m}$, both constant among all devices. A micrograph of the realized pattern, prior to semiconductor deposition, is shown in Fig. 2b.

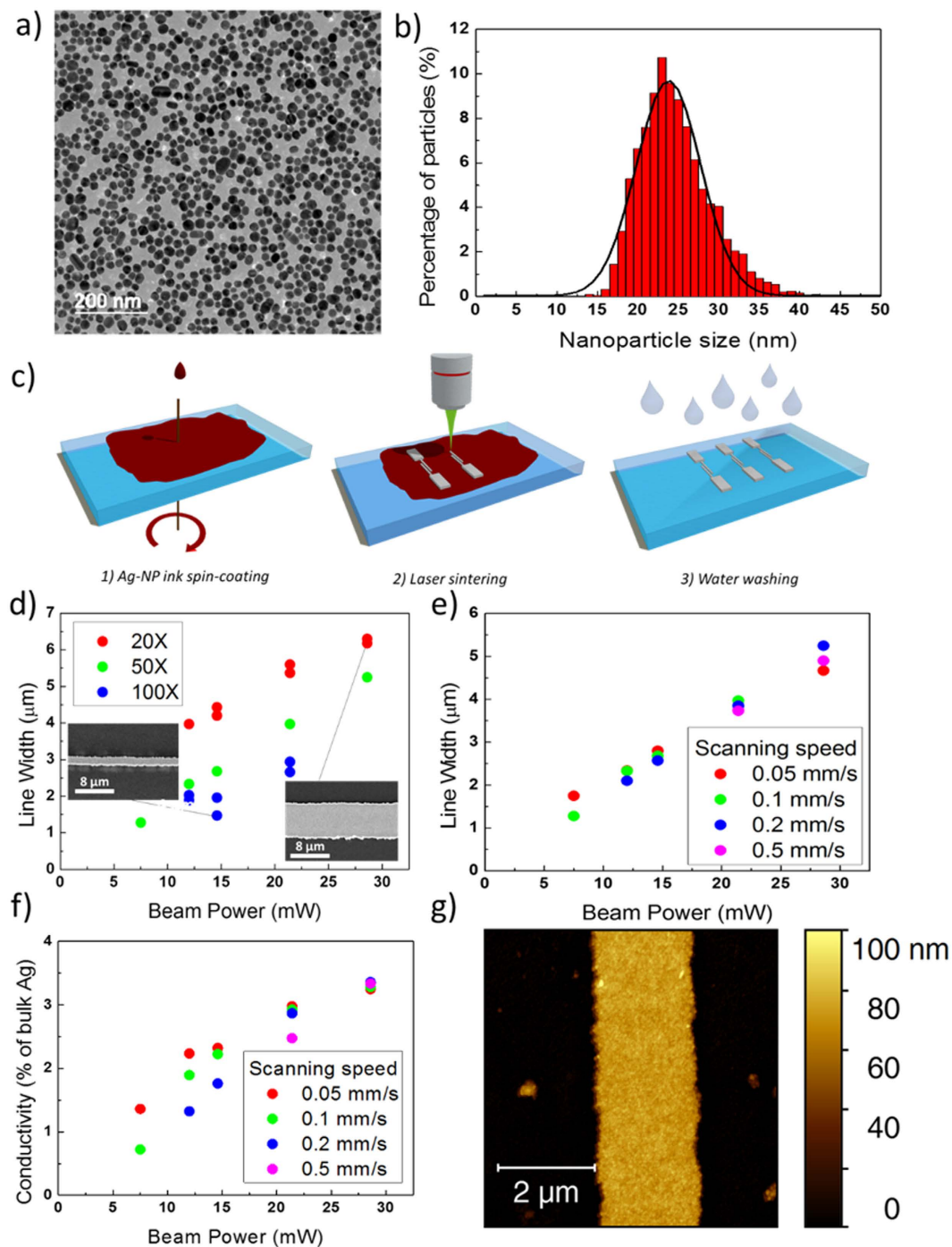


Figure 1. Ag-NP ink properties and fs-laser sintering process. (a) TEM image and (b) nanoparticle size distribution (~ 4500 particles) of the AgNP ink, (c) Scheme of the femtosecond laser sintering process flow, (d) sintered line width vs. beam power for different optics and scan speed 0.1 mm/s (insets show SEM images of some of the lines), (e) sintered line width vs. beam power for different scan speeds (50X optics), (f) sintered line conductivity (relatively to bulk Ag conductivity) vs. beam power for different scan speeds (50X optics) and (g) AFM image of a laser sintered Ag line.

In Fig. 2e and f, we show the measured transfer curves for two long channel devices ($L = 5.1 \mu\text{m}$, red line, and $L = 21.6 \mu\text{m}$, blue line) and for a short-channel device ($L = 1.75 \mu\text{m}$). We summarize in Table 1 the extracted apparent mobilities for the full set of fabricated polymer FETs.

The devices exhibit proper n -type operation and in the linear regime ($V_d = 5 \text{ V}$) the drain current scales accordingly with the reduction of the channel length. The correct scaling is confirmed by the extracted values of linear charge mobility, which remains comparable (in the range $0.1\text{--}0.2 \text{ cm}^2\text{V}^{-1}\text{s}^{-1}$) while the channel length is scaled by one order of magnitude (Figure S2), suggesting good charge injection behavior at the semiconductor/

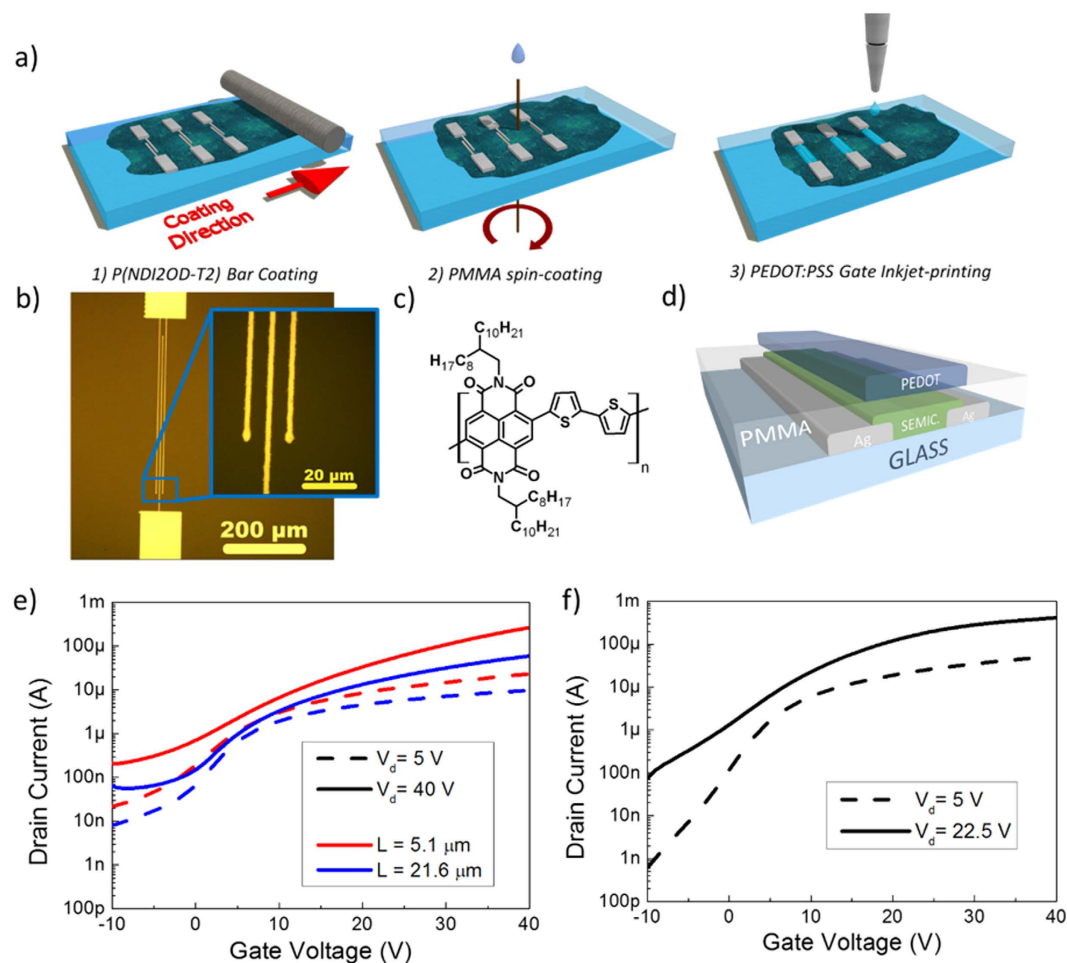


Figure 2. OFET fabrication and DC characterization. (a) Sketch of the fabrication process, (b) optical micrograph of the bottom source and drain electrodes realized through laser sintering, (c) chemical structure of P(NDI2OD-T2), (d) sketch of the realized OFET, and (e) transfer characteristics of two devices with channel lengths $L = 5.1 \mu\text{m}$ and $L = 21.6 \mu\text{m}$ ($W = 800 \mu\text{m}$) and (f) transfer characteristic of a short-channel device ($L = 1.75 \mu\text{m}$, $W = 800 \mu\text{m}$).

Channel length [μm]	Linear mobility [$\text{cm}^2\text{V}^{-1}\text{s}^{-1}$]	Saturation mobility [$\text{cm}^2\text{V}^{-1}\text{s}^{-1}$]
1.75	0.13	0.82*
5.1	0.14	0.74
21.6	0.22	0.37

Table 1. Extracted mobilities for the laser sintered OFETs. * $V_g = 22.5 \text{ V}$.

contact interface. We performed a first approach estimation based on the Transfer Line Method (TLM) method, which can slightly underestimate the contact resistance for the semiconductor in use⁴⁸, and found a normalized contact resistance $R_c W = 7.3 \text{ k}\Omega\text{cm}$ at $V_g = 40 \text{ V}$ (Figure S1), indicating that the scaled electrodes fabricated with our method inject and collect charges effectively.

In the saturation regime we extracted good effective mobilities of $0.37 \text{ cm}^2\text{V}^{-1}\text{s}^{-1}$ and $0.74 \text{ cm}^2\text{V}^{-1}\text{s}^{-1}$ for the devices with $L = 21.6 \mu\text{m}$ and $L = 5.1 \mu\text{m}$ respectively ($V_g = V_d = 40 \text{ V}$), and a high effective mobility of $0.82 \text{ cm}^2\text{V}^{-1}\text{s}^{-1}$ ($V_g = 22.5 \text{ V}$; $V_d = 40 \text{ V}$) in the case of the shortest channel length of $1.75 \mu\text{m}$. In the latter case, we observed a breakdown of the device at currents above $0.9 \mu\text{A}/\mu\text{m}$ when $V_d = 40 \text{ V}$ and $V_g > 25\text{--}30 \text{ V}$, so we limited the driving voltage accordingly, below the onset of breakdown. We remark how the measured effective mobilities in the saturation regime increase when shortening the channel length, in contrast with the behavior exhibited by the linear regime. In fact, we identified a gate dependence of the charge mobility in the saturation regime whose effect is amplified at shorter channel lengths (Figure S3). This behavior is not unique to our work, it is general for the semiconductor in use, it characterizes several high mobility donor-acceptor copolymers recently reported and it can be explained by an effect of the lateral field on injection and/or transport^{49–51}.

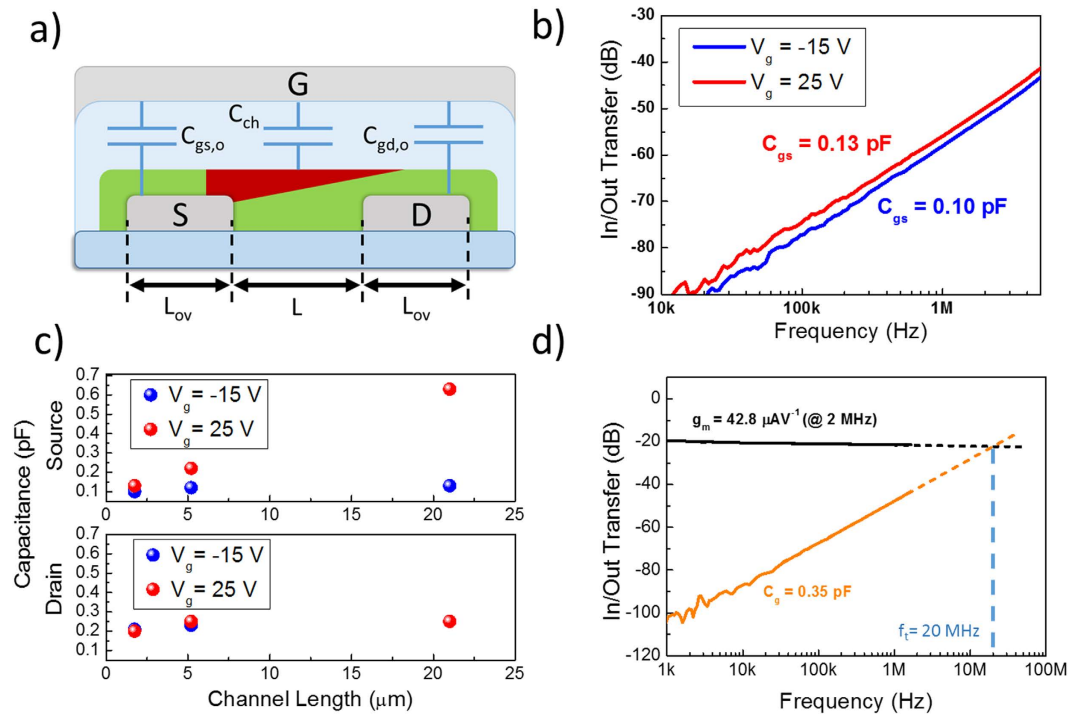


Figure 3. AC characterization of high-frequency OFETs. (a) Sketch of the lateral view of the realized OFETs, highlighting the different capacitances insisting across the device electrodes, (b) measured C_{gs} in depleted-channel ($V_{gs} = -15$ V, $V_{ds} = -15$ V) and in accumulated-channel ($V_{gs} = 25$ V, $V_{ds} = 25$ V) regimes for an n-type device ($L = 1.75$ μm), (c) measured source and drain capacitances for different channel lengths in depleted- and accumulated-channel regimes and (d) determination of the transition frequency for a device ($V_{gs} = 30$ V, $L = 1.75$ μm).

Polymer FETs AC characterization and high-frequency operation. The successful adoption of high resolution fs-laser sintered contacts in polymer FETs allowed us to assess the impact on the maximum operational frequency of the fabricated devices. First, it is worth recalling that, at a first approximation, the final limitation to the speed of a FET is determined by the charge carrier transit time across the channel: $t_{tr} = \frac{L}{v} = \frac{L}{\mu E} = \frac{L^2}{\mu V}$, where v is the carrier velocity, E is the lateral electric field across the channel and V is the drain-to-source voltage. However, additional parasitism intervenes to reduce the actual maximum operational frequency well below this limit. In particular, the overlap capacitances insisting between gate and source/drain electrodes are the most critical in the low-resolution architectures (e.g. tens of μm for inkjet-printed contacts) typically adopted in organic FETs fabrications. A more appropriate figure of merit to describe the maximum operational frequency of a FET is the transition frequency f_t , corresponding to the frequency at which the total AC gate, or “input”, current i_g becomes equal to the AC drain, or “output” current i_d . f_t depends on the device transconductance g_m and on the gate/source and gate/drain capacitances C_{gs} and C_{gd} according to the expression²⁵

$$f_t = \frac{g_m}{2\pi(C_{gs} + C_{gd})} \quad (1)$$

In order to extract f_t , we measured separately C_{gs} , C_{gd} and g_m as a function of frequency for our devices. Details on the extraction methodology can be found in the Supporting Information (SI). Source and drain capacitances were measured both by operating the FETs at $V_g = -15$ V and $V_d = -15$ V (off-state regime), when we expect to probe only the physical overlap capacitances, and at $V_g = 25$ V and $V_d = 25$ V (on-state, saturation regime), when we expect an increased capacitance, due to the accumulated channel region. In Fig. 3b we show the measured C_{gs} in both regimes for a device with $L = 1.75$ μm : in off-state regime a capacitance of 0.10 pF is measured, which is in very good agreement with the theoretical value of 0.096 pF, calculated for a parallel-plates capacitor model with an area corresponding to the geometrical overlap between the source and gate. When accumulating the channel, we measured a capacitance increase of 0.03 pF, which is attributed to the addition of the channel area to the electrodes overlap capacitance. We measured the gate-source capacitance in the saturation regime for different channel lengths and linearly fitted the measured data (Figure S4). The intercept of the fitted line at $L = 0$ μm , identifying the capacitance attributed to the overlap between the contacts, returns 0.085 pF, consistently with the measured and theoretically calculated values. The slope of the fitted line, representing the accumulated channel capacitance per unit channel length, returns 0.026 pF/ μm . If C_{diel} is the dielectric capacitance per unit area, this slope can be theoretically estimated as $\frac{C_{ch,sat}}{L} = \frac{2}{3}WC_{diel} = 0.034$ pF/ μm^2 , which is in good agreement with the fitting. We also measured the gate-drain capacitance in the saturation regime: C_{gd} is equal both in accumulation and in the off-state,

f_t [MHz]	Ref.	Semiconductor		Voltage [V]	Mobility [$\text{cm}^2\text{V}^{-1}\text{s}^{-1}$]
With the use of photolithography/masks					
27.7	29	C60	Evaporated	20	2.22
25	32	Rubrene	Single Crystal	-15	10.3
20	30	C_{10} -DNTT	Evaporated	-20	0.4
20	34	DNTT	Evaporated	-15	0.44
19	33	C_{10} -DNTT	Evaporated	-10	2.5
11.4	29	Pentacene	Evaporated	-20	0.73
10	30	C_{10} -DNTT	Sol. Crystallized ⁵⁶	-20	0.4
3.7	57	DNTT	Evaporated	-3	0.7
1.5–2	23	PBTOR	Spin-coated	-4	2.5
Direct-written electrodes					
20	This work	P(NDI2OD-T2)	Printed (bar-coating)	30	0.9
3.3	36	P(NDI2OD-T2)	Printed (inkjet)	30	0.005
2.8	36	DPPT-TT	Printed (inkjet)	-25	0.024
1.6	25	pBTTT	Spin-coated	-8	0.1

Table 2. Properties and fabrication techniques for the polymer FETs with the highest reported transition frequencies (listed mobility values are to be considered effective parameters, largely depending on the specific device architecture).

corresponding to 0.21 pF for the shortest channel length and consistently with the fact that, in this regime, we are only probing the gate/drain overlap capacitance. The good agreement between the measurements and theoretical value of C_{gd} is obtained also for longer channel lengths. All capacitance data, both for C_{gd} and C_{gs} , have been summarized in Fig. 3c. We measured the transconductance of the short-channel device in the range 1 kHz–2 MHz. Differently from the ideal behavior, a slight roll-off of this figure with frequency can be identified which reduces g_m from $52.8 \mu\text{AV}^{-1}$ at 1 kHz to $42.8 \mu\text{AV}^{-1}$ at 2 MHz (Fig. 3d, black solid line). The maximum frequency limitation of the setup prevented the measurement of the transconductance beyond 2 MHz, and we determined the transition frequency by linearly extrapolating the measured trends of g_m and C_g . In Fig. 3d we show the measurement and the determined $f_t = 20$ MHz. A simple calculation from the measured g_m at 1 kHz and the measured C_g according to (1), would return an $f_t = 24.7$ MHz. Recalling the discussion above, we validate our result by comparing the frequency obtained by AC measurements with the ultimate limit defined by the transit time of the carriers across the channel: for our shortest-channel device we obtain $t_{tr} = 0.9$ ns corresponding to an ideal cutoff frequency of $f_{tr} = \frac{1}{2\pi t_{tr}} = 170$ MHz. The extrapolated f_t is well below the calculated cut-off frequency due to the carrier transit time, thus our estimation is not undermined by the extrapolation method.

Discussion

In Table 2 we compare the result obtained in this work with previous works in which the transition frequency has been explicitly measured, and we report, along with f_t , other relevant figures of merit (i.e. operational voltage and effective mobility) and fabrication details of the devices. Please note that the reported mobility values are effective parameters, largely influenced by the specific architecture adopted, as well as by the semiconductor processing method and microstructure. To the best of our knowledge, our demonstration reaches the highest f_t reported for an *n*-type printed polymer device so far³⁶, and of the same order of magnitude of the highest reported in the organic electronics literature in absolute terms, including devices realized through process flows including photolithography or evaporation steps. Overall, we demonstrate the fastest organic FET fabricated to date without the use of any mask and by combining only printing and direct-writing processes.

The strong enhancement of this figure of merit with respect to previous works dedicated to maskless fabrication of organic electronics, limited to 3.3 MHz in the best case³⁶, is ascribed to multiple contributions. The drastic improvement in the resolution for the definition of the FETs source and drain contacts, owing to the use of fs-laser sintered high-conductive AgNP electrodes, is combined with the bar-coating of an optimized semiconductor morphology² enabling enhanced effective field-effect mobility, also thanks to good charge injection properties of such electrodes. The aforesaid fabrication strategy improves the patterning resolution of a typical direct-writing technique, e.g. inkjet printing, by more than 10 times^{4,53} and obeys the multiple role of reducing both the transistor channel length and the parasitic capacitance present between these electrodes and the gate. Moreover, the proposed process retains additional room for improvement in terms of reduction of the parasitic capacitance, for example with the integration of a self-alignment technique for the patterning of the gate electrode⁵⁴.

In addition to properly controlling the transistor features that are critical for high-frequency operation, the selected fabrication techniques have strong potential for scalability to mass production, featuring both screen-to-screen and roll-to-roll compatibility⁵⁵. The fs-laser process necessitates only of a limited beam power (as low as 10 mW), hence throughput can be enhanced through parallelization of different beams, independently driven (possibly by galvo-scanners), generated from the same laser source. A further possibility for the improvement of the throughput is the adoption of Spatial Light Modulators, which may enable the possibility to write sections of a device or a circuit in a single step. Additionally, we recall that, in a practical application, only a fraction of the features needs to be defined with a high resolution, so that the effective throughput can be further

enhanced. In perspective, these features enable the applicability of the proposed process to large-volumes manufacturing at reduced cost of circuits incorporating polymer transistors operating beyond 20 MHz, therefore widely expanding possible applications of cheap flexible electronics.

Methods

General (NP-ink synthesis). All reagents were purchased from Sigma-Aldrich, and used without further purification: silver nitrate (nr. 209139, ACS reagent, $\geq 99.0\%$), tannic acid (nr. 403040, ACS reagent), sodium citrate tribasic dehydrate (nr. 71402, BioUltra, $\geq 99.5\%$), polyvinylpyrrolidone (nr. PVP10, average m.w. 10 kDa). All glassware employed for AgNP preparation was cleaned with conc. HNO_3 and rinsed with plenty of water. Ultrapure deionized water (Millipore purification system, $18.2 \text{ M}\Omega \text{ cm}$) was used for the preparation of all aqueous solutions. All solutions used for nanoparticle preparation were filtered through a $0.2 \mu\text{m}$ membrane filter (Whatman, cellulose acetate). AgNPs were characterized by Dynamic Light Scattering (DLS) (Zetasizer Nano ZS, Malvern Instruments). AgNP diameter was measured via TEM (JEOL JEM-1011 transmission electron microscope operating at an accelerating voltage of 100 kV). UV/Vis spectra and fluorescence measurements were carried out using a TECAN Infinite M200 Pro plate reader. The concentration of silver in the inks was determined via ICP-OES (Agilent 720 ICP-OES).

Nanoparticle synthesis. Silver nitrate (1.274 g, 7.50 mmol) was dissolved in 1.45 L of water. The solution was heated up with efficient stirring and protected from light until it started to reflux followed by quick addition of 50 mL of a freshly prepared solution of sodium citrate (0.302 M, 15.1 mmol) and tannic acid ($7.35 \times 10^{-4} \text{ M}$, $3.68 \times 10^{-2} \text{ mmol}$) in water. Accordingly, the concentrations of reactants in the reaction mixture were: $[\text{Ag}] = 5.00 \times 10^{-3} \text{ M}$, $[\text{Na citrate}] = 1.00 \times 10^{-2} \text{ M}$, and $[\text{tannic acid}] = 2.45 \times 10^{-5} \text{ M}$. The solution rapidly turned dark indicating nanoparticle formation, but heating was continued for additional 30 minutes. Heating was then removed and the reaction mixture was allowed to reach room temperature overnight. The AgNPs were concentrated by centrifugation (20 min at $10000 \times g$).

PVP-coating of AgNPs. The concentrated AgNPs were redispersed in water containing Polyvinylpyrrolidone (PVP, average m.w. 10 kDa) to afford a 50 mL mixture with $[\text{PVP}] = 6.4 \times 10^{-3} \text{ M}$. This mixture was stirred for 30 min. and then centrifuged 1 h at $10000 \times g$. Most of the supernatant was removed ($>40 \text{ mL}$) and the coating procedure was repeated a second time with overnight incubation. The PVP-coated AgNPs were concentrated to approx. 10 mL by centrifugation (1.5 h at $10800 \times g$) and then washed with water ($2 \times 50 \text{ mL}$) by centrifugation and resuspension. The aqueous AgNP solution was filtered over a $0.2 \mu\text{m}$ cellulose acetate filter before the last centrifugation. The volume of the final PVP-coated AgNP concentrate was approximately 4 mL. Each resuspension step after centrifugation included 20 min. incubation in an ultrasonic bath.

Ink preparation. 2 mL of aqueous PVP-coated AgNP concentrate were added of 16 mL of water. The AgNP suspension was centrifuged (1 h, 20°C at $10800 \times g$), the supernatant removed and the AgNP pellets taken up in 3 mL of water. For this ink: 4.3 mL, 67.1 g/L Ag, DLS: $26.2 \pm 0.2 \text{ nm}$, PDI 0.532, $\lambda_{\text{max}} = 399 \text{ nm}$ (in H_2O), TEM: $23.8 \pm 4.0 \text{ nm}$.

Femtosecond laser sintering setup. The laser setup consists of a commercial laser source (LightConversion PHAROS, based on Yb:KGW as active medium) which generates $\sim 80 \text{ fs}$ -long laser pulses with a repetition rate of 67 MHz, $\lambda = 1030 \text{ nm}$ and maximum output power of 2 W. Before reaching the sample, the beam is conditioned through an optical path which includes a software-controlled attenuator and a focalizing objective (Mitutoyo) lens whose magnifying power can be selected between 20X, 50X or 100X. The sample is positioned on a software-controlled moving stage (Aerotech ABL1000) capable of a maximum resolution of 0.5 nm and a maximum speed of 300 mm/s.

Contacts fabrication. Standard glass slides are used as substrate. They are cleaned in an ultrasonic bath with deionized water, acetone, 2-propanol sequentially for 5 minutes each, then oxygen-plasma treated for 1 min (100 W), and finally heated on a hotplate at 60°C for 5 minutes. The AgNP ink is then spincoated at 1000 rpm for 40s. After laser processing, the sample is rinsed and sonicated for 1 min with deionized water.

Conductive pattern characterization. Optical images are taken with a Zeiss Axio Scope.A1 microscope (100X objective), AFM images are taken with an Agilent 5500 Atomic Force Microscope and SEM images with a JEOL JSM 6010LV. Electrical characterization is performed using an Agilent B1500A Semiconductor Parameter Analyzer.

Organic FETs fabrication. P(NDI2OD-T2) (purchased from Polyera) is dissolved in mesitylene at a concentration of 5 mg/ml. After fabrication of the bottom contacts via laser sintering, P(NDI2OD-T2) is deposited through bar-coating in air atmosphere, using the same process as described in ref. 2. Then poly(methyl methacrylate) (PMMA) is spun from n-butylacetate (concentration 80 mg/ml) at 1500 rpm for 1 minute. After dielectric deposition, the devices are annealed on a hotplate for 30 min at 80°C for residual solvent removal. PEDOT:PSS (Clevios P Jet 700) is patterned over the contacts and channel area via inkjet (using a Fujifilm Dimatix DMP-2831). The devices are then annealed at 120°C in nitrogen atmosphere for 12 h.

Electrical characterization. The devices are measured in nitrogen atmosphere. Static characterization is performed via an Agilent B1500A Semiconductor Parameter Analyzer. Frequency performance was measured using a custom setup which includes an Agilent ENA Vector Network Analyzer and an Agilent B2912A Source Meter. More details on the setup can be found in Supplementary Information.

References

- Baeg, K. J., Caironi, M. & Noh, Y. Y. Toward printed integrated circuits based on unipolar or ambipolar polymer semiconductors. *Adv. Mater.* **25**, 4210–4244 (2013).
- Bucella, S. G. *et al.* Macroscopic and high-throughput printing of aligned nanostructured polymer semiconductors for MHz large-area electronics. *Nat. Commun.* **6**, 8394 (2015).
- Baeg, K. J. *et al.* High Speeds Complementary Integrated Circuits Fabricated with All-Printed Polymeric Semiconductors. *J. Polym. Sci. B Polym. Phys.* **49**, 62–67 (2011).
- Hambusch, M. *et al.* Uniformity of fully gravure printed organic field-effect transistors. *Mater. Sci. Eng. B* **170**, 93–98 (2010).
- Pace, G. *et al.* All-organic and fully-printed semitransparent photodetectors based on narrow bandgap conjugated molecules. *Adv. Mater.* **26**, 6773–6777 (2014).
- Baeg, K. J., Binda, M., Natali, D., Caironi, M. & Noh, Y. Y. Organic light detectors: photodiodes and phototransistors. *Adv. Mater.* **25**, 4267–4295 (2013).
- Jung, Y. *et al.* Fully printed flexible and disposable wireless cyclic voltammetry tag. *Sci. Rep.* **5**, 8105 (2015).
- Emamian, S. *et al.* Fully printed and flexible piezoelectric based touch sensitive skin. *SENSORS, IEEE* 1–4 (2015).
- Voigt, M. M. *et al.* Polymer Field-Effect Transistors Fabricated by the Sequential Gravure Printing of Polythiophene, Two Insulator Layers, and a Metal Ink Gate. *Adv. Funct. Mater.* **20**, 239–246 (2010).
- Mandal, S. *et al.* Fully-printed, all-polymer, bendable and highly transparent complementary logic circuits. *Org. Electron.* **20**, 132–141 (2015).
- Chang, J., Zhang, X., Ge, T. & Zhou, J. Fully printed electronics on flexible substrates: High gain amplifiers and DAC. *Org. Electron.* **15**, 701–710 (2014).
- Dell'Erba, G., Perinot, A., Grimoldi, A., Natali, D. & Caironi, M. Fully-printed, all-polymer integrated twilight switch. *Semicond. Sci. Technol.* **30**, 104005 (2015).
- Kempa, H. *et al.* Complementary Ring Oscillator Exclusively Prepared by Means of Gravure and Flexographic Printing. *IEEE Trans. Electron Devices* **58**, 2765–2769 (2011).
- Schmidt, G. C. *et al.* Fully Printed Flexible Audio System on the Basis of Low-Voltage Polymeric Organic Field Effect Transistors with Three Layer Dielectric. *J. Polym. Sci. B Polym. Phys.* **53**, 1409–1415 (2015).
- Heremans, P. Electronics on plastic foil, for applications in flexible OLED displays, sensor arrays and circuits. *Active-Matrix Flatpanel Displays and Devices (AM-FPD), 2014 21st International Workshop on*, 1–4 (2014).
- Facchetti, A. Printed diodes operating at mobile phone frequencies. *Proc. Nat. Acad. Sci. USA* **111**, 11917–11918 (2014).
- Zhang, J. *et al.* Flexible indium-gallium-zinc-oxide Schottky diode operating beyond 2.45 GHz. *Nat. Commun.* **6**, 7561 (2015).
- Sani, N. *et al.* All-printed diode operating at 1.6 GHz. *PNAS* **111**, 11943–11948 (2014).
- Myny, K. *et al.* Organic RFID transponder chip with data rate compatible with electronic product coding. *Org. Electron.* **11**, 1176–1179 (2010).
- Subramanian, V. *et al.* Progress Toward Development of All-Printed RFID Tags: Materials, Processes, and Devices. *Proc. IEEE* **93**, 1330–1338 (2005).
- Li, J. *et al.* A stable solution-processed polymer semiconductor with record high-mobility for printed transistors. *Sci. Rep.* **2**, 754 (2012).
- Minemawari, H. *et al.* Inkjet printing of single-crystal films. *Nature* **475**, 364–367 (2011).
- Senanayak, S. P. *et al.* Self-Assembled Nanodielectrics for High-Speed, Low-Voltage Solution-Processed Polymer Logic Circuits. *Adv. Electron Mater* **1**, 1500226 (2015).
- Senanayak, S. P. & Narayan, K. S. Strategies for Fast-Switching in All-Polymer Field Effect Transistors. *Adv. Funct. Mater.* **24**, 3324–3331 (2014).
- Caironi, M., Noh, Y. Y. & Sirringhaus, H. Frequency operation of low-voltage, solution-processed organic field-effect transistors. *Semicond. Sci. Technol.* **26**, 034006 (2011).
- Natali, D. & Caironi, M. Charge injection in solution-processed organic field-effect transistors: physics, models and characterization methods. *Adv. Mater.* **24**, 1357–1387 (2012).
- Ante, F. *et al.* Contact resistance and megahertz operation of aggressively scaled organic transistors. *Small* **8**, 73–79 (2012).
- Xu, Y. *et al.* How small the contacts could be optimal for nanoscale organic transistors? *Org. Electron.* **14**, 1797–1804 (2013).
- Kitamura, M. & Arakawa, Y. High Current-Gain Cutoff Frequencies above 10 MHz in n-Channel C60 and p-Channel Pentacene Thin-Film Transistors. *Jpn. J. Appl. Phys.* **50**, 01BC01 (2011).
- Uemura, T. *et al.* Split-gate organic field-effect transistors for high-speed operation. *Adv. Mater.* **26**, 2983–2988 (2014).
- Zschieschang, U. *et al.* Megahertz operation of flexible low-voltage organic thin-film transistors. *Org. Electron.* **14**, 1516–1520 (2013).
- Uno, M. *et al.* High-speed organic single-crystal transistors gated with short-channel air gaps: Efficient hole and electron injection in organic semiconductor crystals. *Org. Electron.* **14**, 1656–1662 (2013).
- Nakayama, K. *et al.* High-Mobility Organic Transistors with Wet-Etch-Patterned Top Electrodes: A Novel Patterning Method for Fine-Pitch Integration of Organic Devices. *Adv. Mater. Interfaces* **1** (2014).
- Uno, M., Cha, B.-S., Kanaoka, Y. & Takeya, J. High-speed organic transistors with three-dimensional organic channels and organic rectifiers based on them operating above 20MHz. *Org. Electron.* **20**, 119–124 (2015).
- Kang, H., Kitsomboonloha, R., Jang, J. & Subramanian, V. High-performance printed transistors realized using femtoliter gravure-printed sub-10 μm metallic nanoparticle patterns and highly uniform polymer dielectric and semiconductor layers. *Adv. Mater.* **24**, 3065–3069 (2012).
- Higgins, S. G. *et al.* Self-aligned organic field-effect transistors on plastic with picofarad overlap capacitances and megahertz operating frequencies. *Appl. Phys. Lett.* **108**, 023302 (2016).
- Kang, H. *et al.* Megahertz-class printed high mobility organic thin-film transistors and inverters on plastic using attoliter-scale high-speed gravure-printed sub-5 μm gate electrodes. *Org. Electron.* **15**, 3639–3647 (2014).
- Khim, D. *et al.* Simple bar-coating process for large-area, high-performance organic field-effect transistors and ambipolar complementary integrated circuits. *Adv. Mater.* **25**, 4302–4308 (2013).
- Hong, S. *et al.* Nonvacuum, maskless fabrication of a flexible metal grid transparent conductor by low-temperature selective laser sintering of nanoparticle ink. *ACS Nano* **7**, 5024–5031 (2013).
- Son, Y. *et al.* Application of the specific thermal properties of Ag nanoparticles to high-resolution metal patterning. *Thermochim. Acta* **542**, 52–56 (2012).
- Son, Y. *et al.* Nanoscale electronics: digital fabrication by direct femtosecond laser processing of metal nanoparticles. *Adv. Mater.* **23**, 3176–3181 (2011).
- Dadosh, T. Synthesis of uniform silver nanoparticles with a controllable size. *Mater. Lett.* **63**, 2236–2238 (2009).
- Bastús, N. G., Merkoçi, F., Piella, J. & Puentes, V. Synthesis of Highly Monodisperse Citrate-Stabilized Silver Nanoparticles of up to 200 nm: Kinetic Control and Catalytic Properties. *Chem. Mater.* **26**, 2836–2846 (2014).
- Cao, Y. *et al.* Syntheses and Characterization of Nearly Monodispersed, Size-Tunable Silver Nanoparticles over a Wide Size Range of 7–200 nm by Tannic Acid Reduction. *Langmuir* **30**, 3876–3882 (2014).
- Zhang, Z. *et al.* Controllable synthesis of silver nanoparticles in hyperbranched macromolecule templates for printed flexible electronics. *RSC Adv.* **5**, 17931–17937 (2015).

46. Tekin, E., Smith, P. J. & Schubert, U. S. Inkjet printing as a deposition and patterning tool for polymers and inorganic particles. *Soft Matter* **4**, 703–713 (2008).
47. Ko, S. H. *et al.* All-inkjet-printed flexible electronics fabrication on a polymer substrate by low-temperature high-resolution selective laser sintering of metal nanoparticles. *Nanotechnology* **18**, 345202 (2007).
48. Caironi, M. *et al.* Efficient charge injection from a high work function metal in high mobility n-type polymer field-effect transistors. *Appl. Phys. Lett.* **96**, 183303 (2010).
49. Luzio, A., Criante, L., D'Innocenzo, V. & Caironi, M. Control of charge transport in a semiconducting copolymer by solvent-induced long-range order. *Sci. Rep.* **3**, 3425 (2013).
50. Sirringhaus, H. 25th anniversary article: organic field-effect transistors: the path beyond amorphous silicon. *Adv. Mater.* **26**, 1319–1335 (2014).
51. Fazzi, D. & Caironi, M. Multi-length-scale relationships between the polymer molecular structure and charge transport: the case of poly-naphthalene diimide bithiophene. *PCCP* **17**, 8573–8590 (2015).
52. Zaki, T. *et al.* Accurate Capacitance Modeling and Characterization of Organic Thin-Film Transistors. *IEEE Trans. Electron Devices* **61**, 98–104 (2014).
53. Sirringhaus, H. *et al.* High-Resolution Inkjet Printing of All-Polymer Transistor Circuits. *Science* **290**, 2123–2126 (2000).
54. Vilkman, M., Ruotsalainen, T., Solehmainen, K., Jansson, E. & Hiitola-Keinanen, J. Self-Aligned Metal Electrodes in Fully Roll-to-Roll Processed Organic Transistors. *Electronics* **5**, 2 (2016).
55. Spyropoulos, G. D. *et al.* Flexible organic tandem solar modules with 6% efficiency: combining roll-to-roll compatible processing with high geometric fill factors. *Energy Environ. Sci.* **7**, 3284–3290 (2014).
56. Nakayama, K. *et al.* Patternable solution-crystallized organic transistors with high charge carrier mobility. *Adv. Mater.* **23**, 1626–1629 (2011).
57. Zaki, T. *et al.* S-Parameter Characterization of Submicrometer Low-Voltage Organic Thin-Film Transistors. *IEEE Electron Device Lett.* **34**, 520–522 (2013).

Acknowledgements

The authors are thankful to: Krishna Chaitanya Vishunubhatla and Luigino Criante for the support with the femtosecond laser machining setup; Sadir Bucella for very useful help in the early stage of the research; to Michele Giorgio for assistance in the fabrication of part of the reported devices. This work has been financially supported by the European Research Council (ERC) under the European Union's Horizon 2020 research and innovation programme 'HEROIC', grant agreement 638059.

Author Contributions

A.P. and M.C. designed the experiments. A.P. performed the experiments on the Ag-NP ink deposition, fs-laser sintering process characterization, OFET fabrication and DC and AC characterization. P.K., M.A.M., P.P.P., R.F. synthesized the Ag-NP ink. All authors analyzed the data and contributed to the manuscript.

Additional Information

Supplementary information accompanies this paper at <http://www.nature.com/srep>

Competing financial interests: The authors declare no competing financial interests.

How to cite this article: Perinot, A. *et al.* Direct-written polymer field-effect transistors operating at 20 MHz. *Sci. Rep.* **6**, 38941; doi: 10.1038/srep38941 (2016).

Publisher's note: Springer Nature remains neutral with regard to jurisdictional claims in published maps and institutional affiliations.



This work is licensed under a Creative Commons Attribution 4.0 International License. The images or other third party material in this article are included in the article's Creative Commons license, unless indicated otherwise in the credit line; if the material is not included under the Creative Commons license, users will need to obtain permission from the license holder to reproduce the material. To view a copy of this license, visit <http://creativecommons.org/licenses/by/4.0/>

© The Author(s) 2016